Acoustic versus aerodynamic installation effects on a generic propeller-driven flying architecture

Michel Roger ⑩, **Daniel Acevedo-Giraldo** ⑩ **and Marc C Jacob** ⑩

Abstract

The present work addresses the combined aerodynamic and acoustic installation effects observed as a subsonic propeller is partly crossing the near-wake of a wing. Only the tonal noise at multiples of the blade passing frequency is considered. The aerodynamic effect is the onset of additional sound sources caused by blade-wake interaction, compared to the case of the isolated propeller. The acoustic effect is the scattering by the wing. The work is aimed at demonstrating the ability of analytical models to estimate separately these effects, which is of primary interest for the pre-liminary design steps of a system. A basic experiment carried out in an anechoic, open-jet facility, is described, for validation purposes. The far-field sound measurements are compared to the pre-dictions and some key outcomes are presented. In particular, the model provides guidelines to avoid configurations of excessive noise.

Introduction

In 1969, J.E. Ffowcs Williams & D.L. Hawkings published a paper of considerable importance for the aeroacoustic community, essentially stating that the sound radiated by arbitrarily moving bodies in the presence of turbulent flow can be thought of as produced by equivalent monopoles, dipoles and quadrupoles.[1] The mathematical formulation was in the continuation of Lighthill's acoustic analogy[2] and its extension by Curle.[3] The same year, they also published another basic article on rotating blade noise,[4] completing some developments made by Lowson[5] about sources in motion.

Univ. Lyon, École Centrale de Lyon, CNRS, Univ. Claude Bernard Lyon 1, INSA Lyon, LMFA, Écully, France

Corresponding author:
Michel Roger, Université de Lyon, École Centrale de Lyon, CNRS, Université Claude Bernard Lyon 1, INSA Lyon, LMFA, UMR 5509, Avenue Guy de Collongue, Ecully 69130, France.
Email: michel.roger@ec-lyon.fr

Both became an important background, in particular for analytical modeling and for the derivation of scaling laws based on dimensional analysis. The present study is aimed at showing how this pioneering view is still of great usefulness, in particular at the early design stage of a mechanical system, in the context of innovative, installed or distributed propulsion systems.

New architectures for future generations of flying vehicles, such as drones, urban air taxis, and so on, have received attention during the past few years. Whatever their use and operational constraints could be, the associated rotating-blade technology will possibly imply innovative installation strategies, raising the question of the acoustic signature. At the early stage of development, for instance when urban authorities have to plan traffic or assess the nuisance, very simple and fast prediction tools are needed. In the same time, the main physical features of the sound sources, all related to flow features, must be taken into account with a minimum realism, so that relevant predictions are ensured. Within this context, resorting to analytical models is an attractive approach. Analytical modeling requires that the dominant sound-generating mechanisms are previously identified, on the one hand, and that simplifications are accepted for mathematical tractability, both on the flow features and on the geometry, on the other hand. Furthermore, the models must include design parameters for a convincing use in optimization algorithms. The theoretical background for such an approach is provided by the acoustic analogy.

A relevant strategy, suited to the analytical investigation of innovative propulsive architectures, is to define generic configurations, in which, typically, a propeller and a neighboring scattering surface are associated. For mathematical tractability, the surface must be easily defined by iso-values of a coordinate system, in which the Helmholtz equation is separable. It must also remain compatible with the assumption of a uniform base flow, apart from the superimposed distortion. Various classes of such generic problems can be defined, all based on the basic wave equation of the analogy, that can be solved with suited Green's functions. Each mimics a given architecture, or part of it. The very-low frequency test case of small-scale propeller operating close to a rigid cylinder, recently addressed by Cros *et al*,[6] is a particular example, in which a strong installation effect was evidenced. The test was performed with a three-bladed model propeller, the axis of which was parallel to the cylinder axis. The free-field tonal noise of the propeller was found to increase by about 15 dB as the propeller was approached to a very short distance to the cylinder, in such a way that the global area encompassing the propeller and the cylinder cross-section remained acoustically compact. The aerodynamic installation effect, namely the production of Blade-Loading Harmonics (BLH) due to the formation of mean-flow distortions, could be considered as negligible in this case; thus the measured increase was attributed to the acoustic installation effect. Indeed it was recovered by a proper asymptotic expansion of the cylinder Green's function, assuming the same sources on the blades. The effect is related to what is referred to as the "compact" Green's function by Howe.[7] Another configuration is selected in the present work, in which the distortion is reinforced as the propeller approaches the scattering surface, so that the competition between both aerodynamic and acoustic installation effects is less clear a priori. The configuration is made of a propeller partially cutting the wake of a thin rigid strip of infinite span, and placed close to the trailing edge. It is depicted in Figure 1.

Historically, dimensional analysis and analytical modeling were the only available means, facing the lack of accurate numerical tools. The latter and the needed computational resources appeared much later than the theoretical background. Nowadays, dimensional and analytical arguments remain of primary interest at the early design stage, typically when a rotating-blade architecture has still unspecified geometrical details. Their lack of accuracy is balanced by their short computational times. Furthermore, they highlight the underlying physics. The present tribute paper is dealing with a mathematical exercise of didactic interest, based on such an analytical approach, keeping in mind
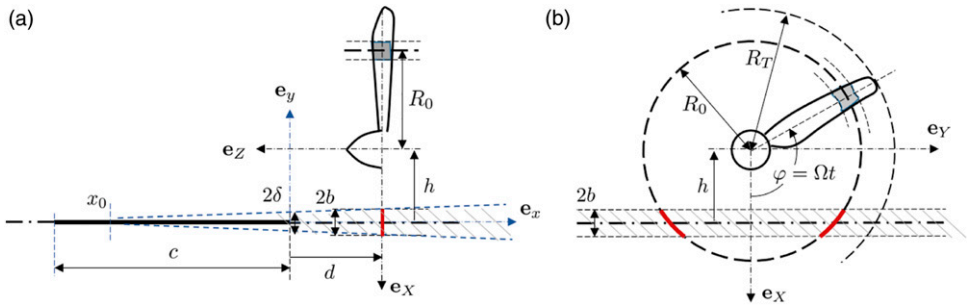
Figure 1. Generic wing-propeller configuration, reference frames and main notations. (a): side view, flow from left to right; (b): front view.

that the approach might be applied as well in the early design stages of a true technological option, and integrated in optimization algorithms.

The paper is organized as follows. Firstly, the generic configuration is depicted and a short dimensional analysis is used to highlight the main parameters of interest. Secondly, the propeller noise formulations used to predict the free-field radiation from a simple distortion model are detailed. Thirdly, the mathematical background of the sound-scattering model is described. Fourthly, a preliminary small-scale experiment carried out in an open-jet anechoic facility, performed to complete the study, is described. Finally, the analysis of results, including comparisons between predicted and measured sound spectra, is presented.

Generic configuration

The selected generic configuration, depicted in Figure 1, includes a thin plate and the associated wake, as well as a subsonic propeller installed at some finite distance from the trailing edge. It could be representative of drones or of future distributed propulsive architectures. The exercise is aimed at exploring two complementary aspects of the positioning of the propeller relative to the trailing edge of the wing, the latter being considered as a scattering screen. As long as the blades actually cross the wake, the effect of approaching the edge is twofold. Firstly, the wake gets deeper and narrower, inducing higher harmonic content and BLH amplitudes, thus higher aerodynamic sound. Secondly, if at least the blade tips enter a small-enough area around the edge, amplification also occurs because of the aforementioned asymptotics of the Green's function, apart from the BLH re-inforcement. The amplification mechanism has been evidenced by Ffowcs Williams & Hall[8] for quadrupoles very close to an edge, in connection with turbulent boundary-layer induced trailing-edge noise. It is less pronounced but still very significant for dipoles, as discussed by Roger *et al*[9] in the context of high-lift device noise. If the blade tips remain outside the wake and boundary layer, as in some over-the-wing configurations, the only effect is the second one and the remaining question is whether the amplification occurs or not. Both aspects make a significant sound increase expected as the propeller distance to the edge is reduced, but the question of which installation effect dominates is probably a matter of combined parameters, which needs to be explored.

Resorting to Vashy-Buckingham's theorem and limiting the scope to a reasonably simplified framework, a functional relationship can be formulated, by which the acoustic pressure p is related to independent parameters as, for instance,

$$\frac{2p}{\rho_0 U_0^2} = \mathcal{F}\left(\mathcal{R}_e, M_0, \xi, \frac{h}{R_0}, \frac{d}{R_0}, \frac{\delta}{R_0}, kR_0, kc\right),$$

where ρ_0 is the fluid density, h and d are the normal and streamwise distances of the propeller center to the edge, respectively, δ the boundary layer thickness at the wing trailing edge, related to the chord c and equal to half the initial wake thickness, $\mathcal{R}_e$ a relevant Reynolds number, M_0 the free-stream Mach number, $\xi = U_0/(\Omega R_0)$ the advance ratio, $k = 2\pi/\lambda$ the acoustic wavenumber associated with the frequency of interest, and R_0 the radius of the considered blade segment. Within the scope of a strip-theory approach, in which the blade is split into spanwise segments, the analysis must be repeated for all segments. A segment is depicted as the gray patches in Figure 1. For the tonal noise addressed in this work, the frequency is a multiple of the blade-passing frequency (BPF) $B\Omega/(2\pi)$, where Ω denotes the rotational speed and B the number of blades. The exact definition of the dimensionless parameters is arbitrary but their number is imposed by the theorem. The functional $\mathcal{F}$ is also unspecified. This statement makes the multidimensional space covered by the generic configuration very wide. Now the present work is focused on the effect of relative positioning for given velocity conditions. Therefore, the Reynolds number can be discarded from the analysis and fixed conditions are selected for the Mach number, the boundary-layer thickness and the advance ratio. Finally, the three leading parameters to be retained for the investigation of the combined aerodynamic and acoustic installation effects are h/R_0, d/R_0 and kR_0. Adding the chord is a matter of available Green's function tailored to the geometry. For arbitrary frequencies in the Helmholtz problem, an exact Green's function is known for a rigid half-plane, that is, a chord extending to infinity upstream. This model is only relevant for very high frequencies, in the limit $kc \gg 1$. This is why an approximate solution is proposed later in this paper to account for a finite chord.

In the strip of radius $r = R_0$, the blade segment is characterized by its chord c_b and span s, and by the stagger angle γ. The velocity triangle relative to the segment, as well as its angle of attack, vary every time it crosses the wake or the boundary layer, and is constant otherwise. Approximating the segment by a flat plate as usually accepted in the linearized thin-airfoil theory, the lift fluctuations result from the projection of the velocity deficit w normal to the chord. Their determination is a separate step, that can be achieved using, for instance, Sears' theory for compact chords and Amiet's theory for non-compact chords.[10] The former is selected here, for simplicity. The exercise could be repeated with refined response functions for non-compact blades. This is not essential for the present investigation, rather dedicated to radiation differences between free-field and installed configurations. Furthermore, the accompanying experiment described later on actually corresponds to compact blade chords.

Free-field sound radiation formulations

Rotor noise formulas and source-mode expansions

Propeller tonal noise is radiated at multiples of the BPF, noted $\omega/(2\pi) = mB\,\Omega/(2\pi)$, where Ω stands for the angular rotational frequency and B the number of blades. Only its dipole sources, responsible for the loading noise,[1] are considered in the present work. At the multiple of order m, and for a blade segment of mean radius r, the complex-valued sound-pressure amplitude at observer point $\mathbf{x}$ reads, with the convention $e^{-i\,\omega t}$ for monochromatic waves,
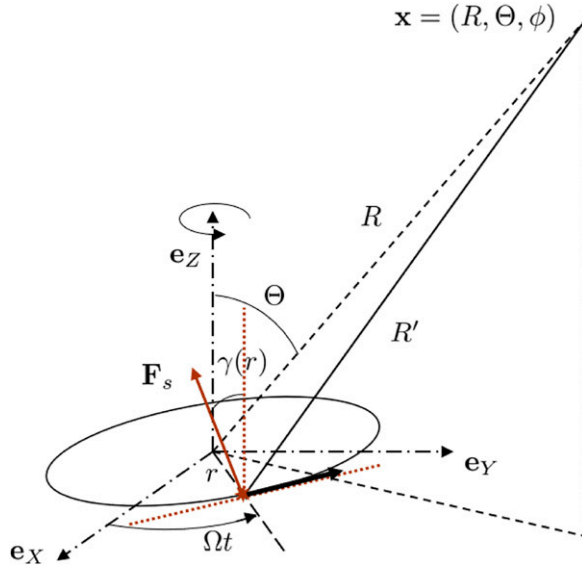
Figure 2. Reference frame attached to a rotating blade segment and associated coordinates.

$$p_{mB}(\mathbf{x}) = \frac{\mathrm{i}k_{mB}r}{4\pi} \sum_{s=-\infty}^{\infty} F_s(r)\{\cos\Theta\cos\gamma(r)\mathrm{G}_{mB-s}^{(1)} + \sin\Theta\sin\gamma(r)\mathrm{G}_{mB-s}^{(2)}\}, \tag{1}$$

with $k_{mB} = mB\,\Omega/c_0$, and

$$\mathrm{G}_n^{(j)} = \frac{\Omega}{2\pi} \int_0^{2\pi/\Omega} \mathrm{G}_j(t)\mathrm{e}^{\mathrm{i}n\Omega t}\mathrm{d}t,$$

$$\mathrm{G}_1(t) = \frac{\mathrm{e}^{\mathrm{i}k_{mB}R'}}{R'^2}\left[1 - \frac{1}{\mathrm{i}k_{mB}R'}\right], \mathrm{G}_2(t) = \sin(\Omega t - \phi)\mathrm{G}_1(t).$$

The expression is valid everywhere in space, as discussed, for instance, in refs. 11, 12. It holds for a pure axial-flow architecture, both terms in the brackets corresponding to the axial and tangential components of the blade force, respectively. $\gamma(r)$ is the stagger angle, defined as the blade-segment inclination with respect to the rotational plane, equivalently the angle between the force and the axial direction. The observer location is defined by its spherical coordinates (R, Θ, ϕ) in the reference frame attached to the circular path of the segment of radius r, featured in Figure 2, as well as the exact source-to-observer distance $R\prime$. The complex-valued factors $F_s(r)$ are the Fourier coefficients of the periodic force on the blade segment, referred to as the BLH.

Each term of the sum defines a free-field radiation mode, of order $n = mB - s$. Its radiating structure expresses the coherent character of the sound sources and the associated interference between blades. The interference is better emphasized with the acoustic and geometric far-field approximation, corresponding to $k_{mB}R\prime \gg 1$ and leading to the expression

$$p_{mB}(\mathbf{x}) = \frac{iBk_{mB}}{4\pi R} e^{i k_{mB} R} \sum_{s=-\infty}^{\infty} F_s(r) e^{in(\phi-\pi/2)} J_n(mBM(r)\sin\Theta) \tag{2}$$

$$\left[\cos\Theta \cos\gamma(r) - \frac{(mB-s)}{mB} \frac{\sin\gamma(r)}{M(r)} \right],$$

noting that $k_{mB} r = mB\, M(r)$, where $M(r) = \Omega r/c_0$ is the tangential Mach number at the current radius. The order n appears as the number of azimuthal lobes of the mode.

The sound field of the mode of order n from the segment of radius r can be exactly reproduced by a continuous circular distribution of stationary dipoles of same radius. For this, the dipoles must have the angle $\gamma(r)$, radiate at the angular frequency $\omega = mB\,\Omega$ and be given the proper phase shift. The dipole strength at azimuth φ along the circle must be defined as $F_s\, e^{in\varphi}$. The circular distribution of equivalent stationary dipoles is called a source-mode. It is discretized as an array of quite a large number of point dipoles for practical implementation.

Introducing the formalism of source-modes as an alternative to equation (1) is well suited to illustrate the formation of acoustic wavefronts from the near-field of distributed sources. For this, the contribution of any point of angle φ along the circle of a source-mode is expressed by the scalar product of the dipole strength by the gradient of the free-space Green's function for the Helmholtz equation. But the interest becomes especially clear when studying the scattering by surrounding surfaces.[11,13] The far-field expression, equation (2), highlights the BLH effectively contributing to a given BPF harmonic. Indeed, the Bessel function rapidly drops to zero as its order exceeds the value of its argument, in absolute values. It operates as a 'band-pass' filter on the BLH spectrum. Furthermore, equation (2) is used to directly compare predictions with measurements, usually carried out with far-field microphones.

Wake model and distortion harmonics

In the present study, the BLH are estimated from an adequate description of the wake velocity profile, using a classical unsteady aerodynamic theory. For simplicity, the wake is assumed symmetric, which means that deflection effects and asymmetry due to wing lift are neglected. The velocity deficit w is a function of the coordinate y normal to the wing plane only. It is modeled by a Gaussian function, as $w(y) = w_0 e^{-y^2/(2\sigma^2)}$. In the reference frame of the propeller and for the strip of mean radius R_0, it is equivalently defined as a function of the angle φ from the X axis in Figure 1, of expression

$$w(\varphi) = w_0 e^{-h^2/(2\sigma^2)} e^{-R_0^2\left[\cos^2\varphi - 2(h/R_0)\cos\varphi\right]/(2\sigma^2)}.$$

This corresponds to a periodic time variation of the velocity triangle associated with the blade segment of same radius, setting $\varphi = \Omega\, t$. The induced blade loading harmonics are directly imposed by the distortion harmonics w_s, defined as

$$w_s = \frac{W_0}{\pi} \int_0^\pi e^{-a^2 \cos^2\varphi + b\cos\varphi} \cos s\varphi\, d\varphi,\ w(t) = \sum_{s=-\infty}^{\infty} w_s e^{is\varphi}, \tag{3}$$

with

$$a = \frac{R_0^2}{2\sigma^2}, b = \frac{R_0 h}{\sigma^2}, W_0 = w_0 e^{-h^2/(2\sigma^2)}.$$

In this simple model, the wake depth w_0 (deficit on the center line) and half width σ are decreasing and increasing functions of the streamwise coordinate x, respectively. The initial value of σ at the edge is imposed by the boundary-layer thickness δ, and the initial depth is equal to the external velocity U_0. Physically consistent models have been made available in the literature for both parameters, with significantly different behaviors for isolated airfoils, linear cascades and rotors or stators. They could be used for parametric studies. In the present work, predictions are made with parameters w_0 and σ directly tuned on measured profiles in the experiment.

Edge scattering model

Half-plane Green's function and amplification regime

The exact Green's function for the Helmholtz equation tailored to a rigid half-plane is commonly used to infer the basic properties of sound scattering by a trailing edge. Two-dimensional formulations, explicitly addressing uniform motion of the fluid and the question of a Kutta condition, are reported by Jones[14] and Rienstra.[15] The three-dimensional Green's function is required for the present application. Its expression in a medium at rest, first given by MacDonald,[16] has been used by Ffowcs Williams & Hall in its far-field approximation,[8] dealing with the scattering of turbulence as sound at a trailing edge. Important results were found, in particular the enhanced radiation of quadrupoles approached very close to the edge. Amplification was evidenced with the factor $(k\varrho_0)^{-1}$ on the acoustic pressure as $k\varrho_0$ goes to zero, ϱ_0 being the source-to-edge distance. This put some light on the essence of trailing-edge scattering of turbulence as sound. The formulation is easily extended to a fluid in uniform motion parallel to the half-plane and normal to its edge, as more recently discussed in ref. 9, where it is also emphasized that the same amplification operates on dipoles, with the factor $(k\varrho_0)^{-1/2}$. In all cases, this compact scattering regime corresponds to a cardioid radiation pattern, independent of the kind of source. In the present investigation, the sources of propeller noise are distributed on a circle of arbitrary radius and distance to the trailing edge. In some cases, some of them can get very close to the edge whereas other remain well apart, leading to some imbalance. The exact formulation of the Green's function is therefore essential.

The original three-dimensional form of the half-plane Green's function in a medium at rest is expressed in cylindrical coordinates, for a source point $\mathbf{x}_0 = (\varrho_0, \vartheta_0, z_0)$ and an observer at point $\mathbf{x} = (\varrho, \vartheta, z)$, the z axis being along the edge and ϑ being π along the half-plane and zero in its continuation (Figure 3). It reads

$$G_{1/2}^{(0)}(\mathbf{x}, \mathbf{x}_0) = \frac{-ik}{4\pi^2} \left\{ \int_{-\infty}^{u_0} \frac{K_1^*\left(ikR_1\sqrt{1+u^2}\right)}{\sqrt{1+u^2}} du + \int_{-\infty}^{u_1} \frac{K_1^*\left(ikR_2\sqrt{1+u^2}\right)}{\sqrt{1+u^2}} du \right\} \qquad (4)$$

where the upper bounds of the integrals are given by

$$u_{0,1} = \pm\frac{2}{R_{1,2}}(\varrho\varrho_0)^{1/2} \cos\frac{\vartheta \mp \vartheta_0}{2}$$
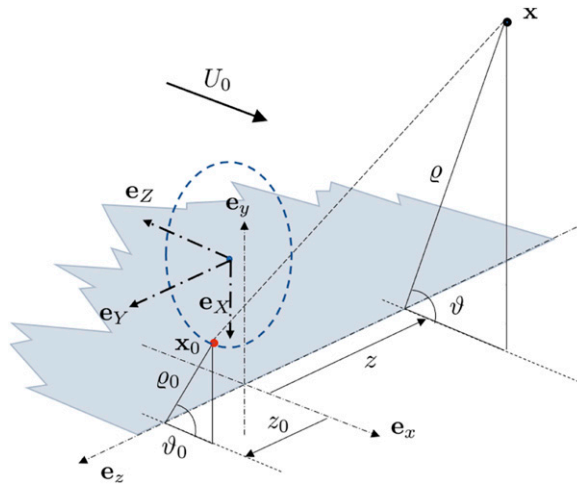
Figure 3. Source and observer coordinates for the half-plane Green's function.

with

$$R_{1,2} = \left[\varrho^2 + \varrho_0^2 + (z - z_0)^2 - 2\varrho\varrho_0\cos(\vartheta \mp \vartheta_0)\right]^{1/2}.$$

K_1 is the modified Bessel function of order 1, equivalently written in terms of the Hankel function as $K_1^*(i\xi) = -(\pi/2)H_1^{(1)}(-\xi)$.

The Green's function with flow is obtained from that without flow by a Lorentz transform, as

$$G_{1/2}^{(M_0)}(\mathbf{x}, \mathbf{x}_0) = \frac{1}{\beta}e^{-iKM_0(X-X_0)}G_{1/2}^{(0)}(\mathbf{X}, \mathbf{X}_0) \tag{5}$$

in which $\mathbf{X}$ and $\mathbf{X}_0$ are coordinate vectors for which the streamwise coordinate x has been replaced by $X = x/\beta$, the wavenumber being rescaled as $K = k/\beta$ with $\beta = \sqrt{1 - M_0^2}$, $M_0 = U_0/c_0$ being the Mach number. The flow is in the direction of the coordinate x.

The exact acoustic field of a point dipole of force $\mathbf{F}$ is given by the scalar product $\mathbf{F} \cdot \nabla G_{1/2}^{(M_0)}$, the derivatives of the Green's function being calculated with respect to source coordinates. Therefore equation (4) is the basis for deriving the uniformly-valid radiated field of arbitrary source distributions accounting for the diffraction by the edge, at the price of a numerical treatment of the integrals.[9]

Finite-chord correction

In the present approach of simplified geometry, considering the finite chord length c in the analysis requires that the rigid half-plane is replaced by an infinite strip of coordinates ($-c \leq x \leq 0$, $-\infty \leq z \leq \infty$). The scattering of a source-mode by the strip may strongly differ from the ideal trailing-edge scattering deduced from the half-plane Green's function, especially if the chord length c is not much larger than the acoustic wavelength λ. Indeed, more sound is regenerated in the shadow region. Furthermore, the interference is incomplete in the reflection region. Such effects must be accounted for when searching for some optimized configurations, which would require the exact Green's function for a strip of arbitrary
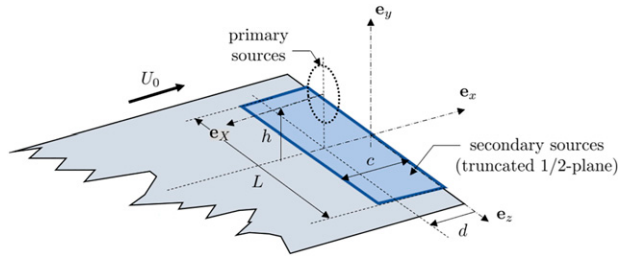
Figure 4. Finite-chord correction of the half-plane scattering problem. Definition of the secondary sources and main notations.

chord. No uniformly-valid, closed-form expression for this Green's function is available to authors' knowledge. High-frequency solutions for the diffraction of an acoustic plane wave by an infinite rigid strip in a fluid at rest, derived with a two-step application of the Wiener-Hopf technique, are reported, for instance, by Noble.[17] For this, two complementary half-plane problems are solved iteratively, the scattering by the second edge being understood as a correction to the scattering by the first edge. But the two-step approach is a high-frequency approximation, typically valid for non-compact chords, that is high values of kc. Higher-order iterations should be determined for moderate values of kc. Moreover, the plane-wave assumption is restrictive. A Green's function for a strip has been derived by Howe, in the case of low Mach numbers and sources close to an edge,[18] using an iterative procedure and a matching with a compact Green's function for low frequencies. These reference solutions only address limit cases. The uniformly valid formalism needed for the present investigation is missing. Therefore, a somewhat empirical correction procedure is proposed in this section, as an alternative. The idea is to reproduce finite chord effects with only minor modifications to the approach detailed in the previous section. It is meant to yield estimates of the leading edge scattering, not exact predictions, in order to address issues such as selecting good candidates for the propeller position and sorting out poor configurations.

The idea, illustrated in Figure 4, can be summarized as follows. In a first step, the total sound from the source-mode is calculated with the half-plane Green's function, but for observer locations distributed over the finite-chord strip. For this, the observer point **x** is approached to the surface $y = 0$ from any side. The source-mode defines the primary sources, the total sound field of which includes the direct field and the scattered field. The latter is obtained by subtracting the former from the total field. According to Green's formalism, the scattered field is exactly the direct field of secondary dipole sources distributed over the strip. The strength of these dipoles per unit area is equal to the acoustic pressure jump between both sides of the strip, after subtracting the direct field. This is equivalent to consider twice the scattered sound pressure at the wall $y = 0^+$. Once the secondary sources are known, their radiation is calculated in a second step with the free-field Green's function and combined with the direct field of the primary sources. This provides a modified total field, in fact an 'incomplete half-plane scattering', hopefully more reliable. Though the final combination of primary and secondary sources is fully relevant, the secondary sources are only approximate, since deduced from a Green's function tailored to the half-plane but not to the strip. Furthermore, the strip must also be truncated spanwise for the practical implementation, with some span length L. This effect is not addressed in the present model, but a dimensional argument suggests that a finite span would not significantly modify the radiation for $L/\lambda \geq 1$ and for observation angles that are not too shallow in the spanwise direction. Validation tests, not detailed here, have been performed in a two-dimensional case including a finite-chord segment and a point dipole source. For this, the approximation has been compared to exact numerical simulations performed with a finite-element code solving the

Figure 5. Sketch of the experimental setup in the ECL low-speed anechoic facility, featuring the vertical wing and the horizontal pylon as gray surfaces. Microphone angle θ_m and distance R_m indicated for the microphone 1. Microphone angles, from 1 to 5: $-113°$, $-83°$, $-53°$, $-23°$ and $+37°$.

convected Helmholtz equation.[19] It was found reliable for source locations in some vicinity of the trailing-edge, which is the scope of the present study.

Small-scale experiment

Experimental setup

A dedicated experiment has been performed in the low-speed, open-jet anechoic wind-tunnel of the École Centrale de Lyon (ECL), for demonstration. In view of the didactic character of the study, a small-scale wing-propeller system of relatively small dimensions, readily handleable, has been defined, with minimum instrumentation. A sketch of the experimental setup featuring the main parameters and axes is shown in Figure 5. The tested propeller is a commercial 3-bladed drone propeller, of tip radius 75 mm, powered by an electric motor Maxon (type 2322.980-52.235-200). The motor is inserted inside a horizontal cylindrical hub fixed to one end of a thin flat pylon. The propeller is installed at zero incidence close to a rectangular flat-plate airfoil aligned with the incident flow, mimicking a wing. This ensures a negligible lift of the wing. The latter is held vertically by narrow bars at its span ends, fixed to the nozzle lips of the square nozzle. The wing leading edge is shifted downstream from the lips by the amount $\Delta_x = 75$ mm. It is also displaced from the middle of the nozzle cross-section, at the distance $\Delta_y = 75$ mm from the right-bank edge, in such a way that the propeller-wing system remains embedded in the potential core of the wind-tunnel jet. The propeller positioning is defined by the plane normal to its axis and cutting the blades at mid chord, referred to as the propeller plane. This choice is logical for unswept twisted blades, justified by the radial piling of the blade cross-sections. The streamwise distance of the propeller plane to the trailing edge of the wing and the normal distance of the propeller axis to the wing chord line, noted d and h, respectively, are adjustable. Positive values of d refer to a propeller plane placed downstream of the edge. The propeller axis and the plate holding the propeller are in the horizontal mid-span plane of the wing.

A horizontal circular array of five microphones B&K 1/2" type 4189 is used to measure the sound in the mid-span plane of the wing. The center of the array is the mid-span point at the trailing edge of the wing. Four microphones are distributed along the right-bank side of the array, which would

Table 1. Main parameters of the tested wing-propeller configurations.

|	Case 1	Case 2	Case 3
d (m)	0.035	0.009	0.009
h (m)	0.072	0.072	0.095
$k\sqrt{d^2 + (h - R_2)^2}$	0.3	0.086	0.2

correspond to the pressure side of the wing and to sound radiation towards the ground in a practical application. Possible sound masking for over-the wing propeller installation corresponds to this area. The fifth microphone is on the left-bank side. The microphone angles θ_m from the direction of the incident stream are $-113°$, $-83°$, $-53°$, $-23°$ and $+37°$. The microphone distance to the trailing edge is $R_m = 1.1$ m. It ensures acoustic far-field conditions beyond 300 Hz. The pylon chord is of 145 mm and its leading edge is recessed by 105 mm from the propeller plane. Extraneous sound sources are expected from the flow over the pylon, including propeller wake impingement. These sources negligibly contribute to the measured sound because they radiate as vertical dipoles, with extinction in the mid-span plane of the wing.

Three test cases are discussed in the present work, the corresponding values of d and h being given in Table 1. In cases 1 and 2, the blade tips intercept the wake of the wing, at farther and closer distances to the edge, respectively. In case 3, the whole propeller is outside the wake. The flow delivered by the nozzle has a residual turbulent intensity below 0.8%. Its velocity is fixed at $U_0 = 11$ m/s and the rotational speed of the propeller is set to 9840 r/min, corresponding to a BPF of 492 Hz $\pm$ 1 Hz. Small variations may be produced when repeating the measurements for various configurations. The tangential tip speed V_t is of 77.3 m/s, and the associated advance ratio U_0/V_t of 0.14. A key parameter for the assessment of edge scattering is the Helmholtz number based on the source-to-edge distance ϱ_0. This number for the blade-tip section, say $k\varrho_0 = k\sqrt{d^2 + (h - R_T)^2}$, is reported in Table 1. In particular, case 2 is expected to involve amplification in the diffraction mechanism, provided that strong-enough aerodynamic noise sources take place at the blade tips.

Sample results

The wake velocity deficit in the wake of the wing has been measured by a Pitot probe, for both interaction distances d in Table 1. The measuring traversing lines have been slightly shifted forward by 3 mm with respect to d, to refer to the leading edge instead of the mid-chord. Indeed, the interaction induces lift fluctuations which concentrate at the leading edge. The results are reported in Figure 6(a), where the velocity deficit is normalized by the outer velocity U_0. As expected, the deficit is thinner and deeper for the shortest interaction distance. It is expected that the lift fluctuations are more impulsive, resulting in an increased sound generation at the high BPF harmonics. Gaussian fits are superimposed on the measured data in Figure 6(a), indicating that the model is consistent. The parameters w_0 and σ are indicated on the plot. A slight asymmetry is noticed between both sides of the wake center line, not believed to result in significant errors when applying the Gaussian model to noise predictions. It is also worth noting that in case 3, the blade tips do not interact with the wake.

The spectra of distortion harmonics w_s predicted with equation (3) are plotted in Figure 6(b) for the two configurations of actual wake cutting, cases 1 and 2. The same envelope is found, wider and higher for the shortest distance d. It is remarkable that, though the velocity deficit is approximated as a Gaussian profile, the oblique and curved crossing by the blade tips generates a BLH-spectrum
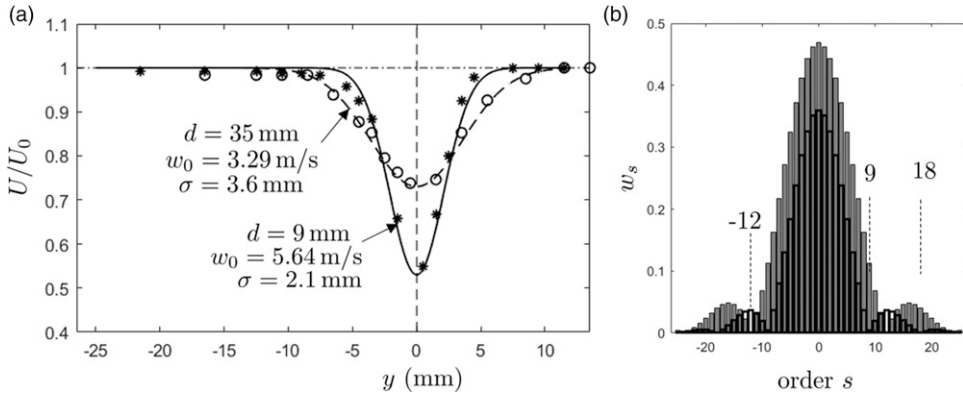
Figure 6. (a): normalized wake velocity deficits as measured by a Pitot probe (symbols) and interpolated by a Gaussian fit. Parameters indicated on the plot. (b): Bar-graph of model distortion harmonics according to equation (3); case 1 (empty thick-black) and case 2 (gray).

envelope which differs from a Gaussian shape, with minima and secondary maxima. The nearly zero value for $s = -12$ in case 2 and the local minima for $s = 9$ and $s = 18$ in case 1 are indicated by vertical dashed lines in Figure 6(b). Each distortion harmonic induces the blade-loading harmonic of same order, the radiation efficiency of which is determined by the Bessel-function factor $J_{mB-s}(mB$ $M\sin\Theta)$, at the BPF harmonic of order m and at the emission angle Θ. Because the factor rapidly goes to zero for orders $n = mB - s$ larger than the argument $mB\,M\sin\Theta$, its effect is to select a limited interval of actually contributing BLH orders, centered at $s = mB$. More sound is therefore expected at higher BPF harmonics in case 2.

Apart from the installed wing-propeller configurations, sound spectra have been measured without the wing, in order to get access to the free-field radiation from the propeller. Complementary measurements have also been performed after removing the propeller and keeping the motor off, which provides an estimate of the background noise, defined as all other contributions than the propeller. This includes the trailing-edge noise of the wing and additional noise due to the flow over the supporting structures. Motor noise has not been characterized; it has been reported as of secondary importance in similar studies, especially if attention must be paid to the tonal noise.[20]

Typical sound spectra for all installed cases and the microphone 3 are reported in Figure 7, where they are compared to the free-field spectrum. The background noise, also shown in red in Figure 7(a), is found responsible for the low-frequency broadband noise, including some peaks attributed to the flow impingement on the support of the microphone array. It becomes negligible at mid-to-high frequencies. Therefore, no correction is needed for the analysis of the tones, unambiguously attributed to the propeller, as their emergence is of several tens of decibels above the background noise at low harmonic orders. It is worth noting that the relative displacements of the propeller are of the order of 2 cm between configurations, so that the variations in propagation distances and wave angles with respect to the microphones remain small, in view of the array radius of 1.1 m. The associated level variations are about 0.16 dB. In such conditions, superimposing sound spectra measured in various configurations, for the sake of comparison, makes sense and lies within the overall accuracy of the measurements.
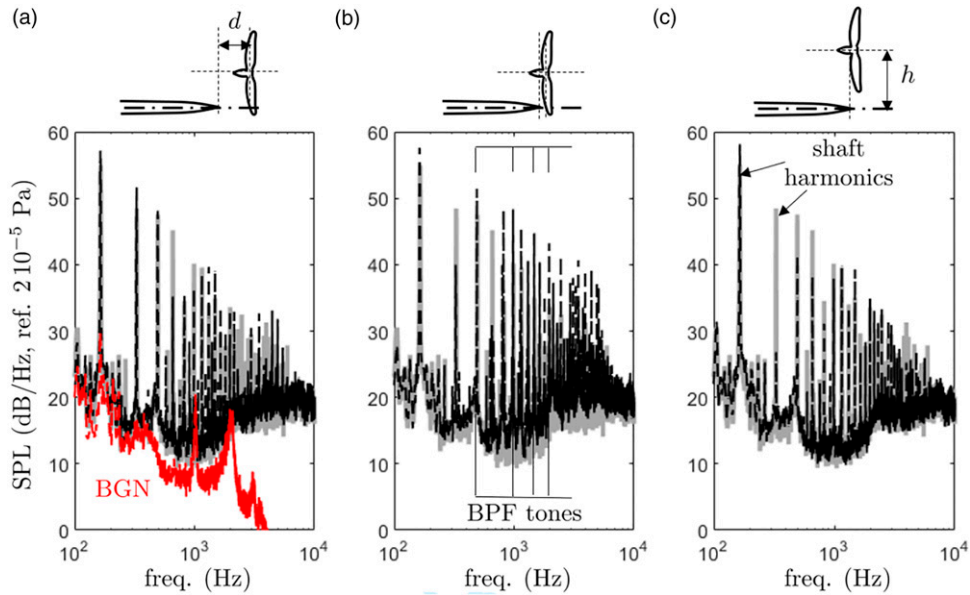
Figure 7. Typical far-field sound spectra for the cases 1 (a), 2 (b) and 3 (c). Installed (black-dashed) versus free-field (gray) configurations. Microphone 3. Background noise plotted in red for comparison in subplot (a).

Analysis of results

Tonal-noise assessment

A clear feature of the present data set is the strong emergence of harmonics of the shaft rotational frequency, which makes the BPF harmonics of interest hard to isolate. The former and the latter are pointed in Figure 7(c) and (b), respectively, for clarity. The shaft harmonics are attributed to mechanical imbalance and to blade-to-blade differences, possibly induced by deformations of the plastic blades. Only the BPF tones are analyzed in the present work. Keeping this in mind, differences in the measured sound spectra for the propeller in free field and in installed configuration, case 3, are mainly attributed to sound scattering by the wing. This is confirmed by some overall similarity, and the same broadband noise spectrum. A richer high-frequency content is observed when successively inspecting cases 3, 1 and 2, which indicates more pronounced aerodynamic installation effects. The analysis of these effects is focused on the BPF tones in the following, which implies a basic procedure to isolate the tones.

Indeed, slight variations of the rotational frequency occur during the acquisition time, exceeding 1 Hz. Furthermore, separate runs in different configurations induce additional variations. Therefore, the power spectral densities of the acoustic pressure have been integrated in intervals of 10 Hz centered on multiples of the BPF (between 490 Hz and 495 Hz), for more relevant tonal-noise comparisons. The results are reported in Figure 8 for the first 10 BPF tones, and the four microphone positions, numbered 1 to 4. The lowest tonal noise is measured in case 3, for which wake cutting by the blades is avoided. Though expected similar to those in case 3, the free-field tonal noise levels are found globally lower, except at the BPF ($m = 1$). Wake interaction in case 1 generates louder sound
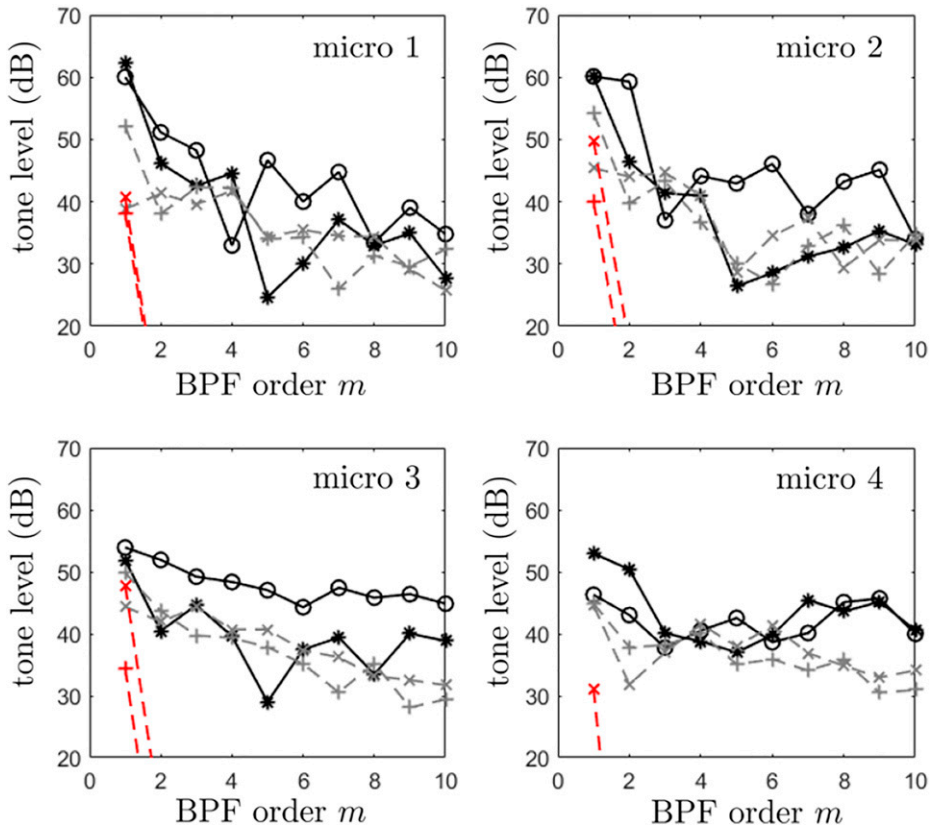
Figure 8. Measured tonal noise levels, after integration over a bandwidth of 10 Hz. (* plain): case 1, (∘ plain): case 2, (× gray): case 3, (+gray): free field. Thickness (- + -) and steady-loading noise (-×-) estimates superimposed for comparison.

at the BPF and its first two or three harmonics, only a slight increase being observed at higher harmonics, except at the microphone four position. This could be due to the shallow angle of this microphone, but is not fully understood yet. Finally, the sound is dramatically increased over the whole investigated range of BPF harmonics in case 2, as expected from a more impulsive interaction with the wake. The overall increase is of about 10–15 dB, except for the microphone 4, located closer to both the propeller axis and the wing plane. Next sections are dedicated to analytical predictions, aimed at elucidating these tonal noise variations. It must be kept in mind that the natural radiation properties of the modes involved in the direct sound radiated by the installed propeller, on the one hand, and their scattering by the wing, on the other hand, combine in an intricate way to determine the measured sound. This competition explains accidents in the envelope of the tonal noise spectrum, as discussed in following sections. For conciseness, the discussions will be fully detailed for the BPF only, in order to illustrate the interest of the general modeling approach.

Table 2. Set of parameters used for steady-loading-and-thickness noise estimates: segment chord c_j and mean radius R_j, stagger angle γ_j and sectional thrust coefficient.

R_j (mm)	10.9	17.6	24.4	31.1	37.9	44.6	51.4	58.1	64.9	71.6
c_j (mm)	11	12.5	13.5	14.5	15.5	16.5	16.5	16	15	13
γ_j (°)	21	33	28	22	18	15	11	9.5	8	6.5
$\partial C_T/\partial r$	0.01	0.02	0.035	0.05	0.07	0.085	0.08	0.07	0.065	0.06

Steady-loading and thickness noise estimates

An important question when addressing the noise from installed propellers is to know whether the thickness noise, on the one hand, and the steady-loading noise, associated with thrust and torque, on the other hand, contribute or not to the total sound. This can be easily recognized from the properties of the Bessel functions involved in the far-field formulation. As pointed out in ref. 12, steady-loading noise is significant, even at relatively low Mach numbers characteristic of drone rotors, for low blade numbers and BPF harmonic orders. However, the envelope of the tonal-noise spectrum is expected to decrease fast and quite regularly, which is obviously not the case in the present free-field measurements.

For practical implementations of both steady-loading noise and thickness noise models, the exact blade cross-section design is required. Because this information is not provided for the commercial propeller, rough estimates are proposed instead in this section. For steady-loading noise, an indicative lift coefficient has been reconstructed for each blade segment, deduced from the sectional thrust distribution reported by Misiorowski *et al*[21] in the case of a drone rotor in forward flight. Only the azimuthally averaged part has been considered, leading to the values reported in Table 2. For thickness noise, only the dipole term of the expansion in dipole and quadrupole distributions in the inner volume of a segment has been considered, according to the formulations in references [1, 22]. The volume of a segment has been assimilated to that of a parallelepiped of $e = 1$ mm-thickness having the local chord c_j and span Δr. Despite their large inaccuracy, expected of a couple of decibels, such estimates are enough for the present discussion. For the segment of mean radius R_j, the steady-loading noise and the thickness noise are predicted from the expressions

$$p_{SL}(\mathbf{x}) = \frac{\mathrm{i} m B^2 \Omega}{4\pi c_0 R} F_0^{(j)} \mathrm{J}_{mB}\big(mBM_j \sin\Theta\big)\left[\cos\gamma_j \cos\Theta - \frac{\sin\gamma_j}{M_j}\right],$$

and

$$p_T(\mathbf{x}) = \frac{m B^2 \Omega}{4\pi c_0 R} F_R^{(j)} \mathrm{J}'_{mB}\big(mBM_j \sin\Theta\big)\sin\Theta,$$

with $F_0^{(j)} = C_L c_j \Delta r \rho_0 (\Omega R_j)^2/2$, and $F_R^{(j)} = \rho_0 c_j e \Delta r \Omega^2 R_j$, respectively.

The first expression is obtained from equation (2); the second one follows the same principles, not detailed here, for a radial force, the strength of which is defined by the centripetal acceleration. Additional phase terms having no effect on the final tone amplitudes have been discarded for clarity. With the present set of characteristic parameters, the obtained values are superimposed in Figure 8 for indicative comparison. The predicted thickness noise and steady-loading noise are found of the same order of magnitude as the measured levels at the BPF in the free-field and case-3 configurations, especially at the microphone positions two and three close to the rotation plane. The fast decrease at higher frequencies makes the levels at 2BPF be outside
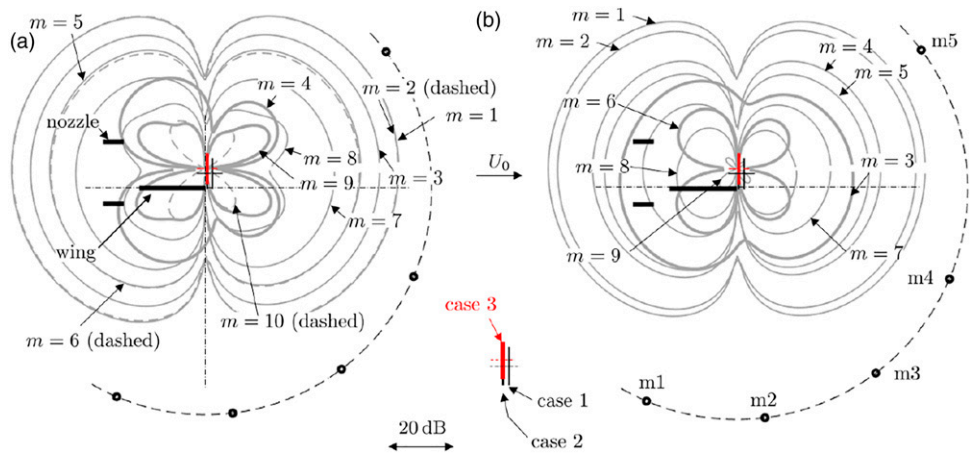
Figure 9. Theoretical free-field directivity patterns of BPF harmonics 1 to 10 (gray plots), superimposed on schematic setup. Microphone positions indicated by the black symbols, nozzle lips and wing-plate shown as thick segments. (a): case 2, (b): case 1. Same relative decibel scale on all plots.

the plotting range. It is conjectured that the slowly decreasing level of higher-order BPF harmonics in case 3 and in free-field is the trace of residual flow distortions. The latter can be attributed to vortices and recirculating flow patterns, around the blade tips and close to the hub. Such patterns have been evidenced by numerical simulations in multi-rotor configurations.[23] Their investigation is beyond the scope of the present study. The importance of steady-loading and thickness noise will be re-addressed at the light of edge scattering in the section dedicated to the scattering model.

Free-field wake-interaction noise predictions

Analytical predictions of the wake-interaction tonal noise are discussed in this section for the first 10 BPF harmonics, based on the free-field formulation, equation (2). Only the last two tip segments of the blades were considered, since other parts are not involved in the interaction, but it has been checked that only the tip segment provides a significant contribution. The BLH are deduced from the Gaussian wake model, tuned on the measurements. Theoretical directivity patterns are first displayed in Figure 9(a) and (b), for the shortest and largest separations, cases 2 and 1, respectively. The diagrams are superimposed in gray on a sketch of the setup elements and of the microphones, for a better view of the measuring positions with respect to sound extinction angles. A globally monotonous decrease of the overall amplitude is found as the BPF order increases, with a singular behavior of some orders. In case 2, the mode $m = 4$ exhibits a four-lobed pattern, with a sudden drop of the noise level, whereas the modes 3, 5 and 6 radiate much more effectively, with the two-lobed pattern characteristic of an axial dipole. The latter is the trace of the symmetric radiation mode, associated with the Bessel function J_0. This behavior results from the special distribution of BLH amplitudes, illustrated in Figure 6(b). Indeed, in case 2, the BLH of orders $s = \pm 12$ are around zero, so that the symmetric mode $n = 4B - s = 12 - 12 = 0$ is switched off, leading to zero sound on axis. In case 1, a local non-zero but minimum BLH amplitude is reached for $s = \pm 9$, which now makes a loss of efficiency expected for the BPF harmonic 3, though less pronounced, compared to the modes 2, 4 and 5. On-axis extinction is also produced in case 1 at the sixth BPF harmonic, because of the
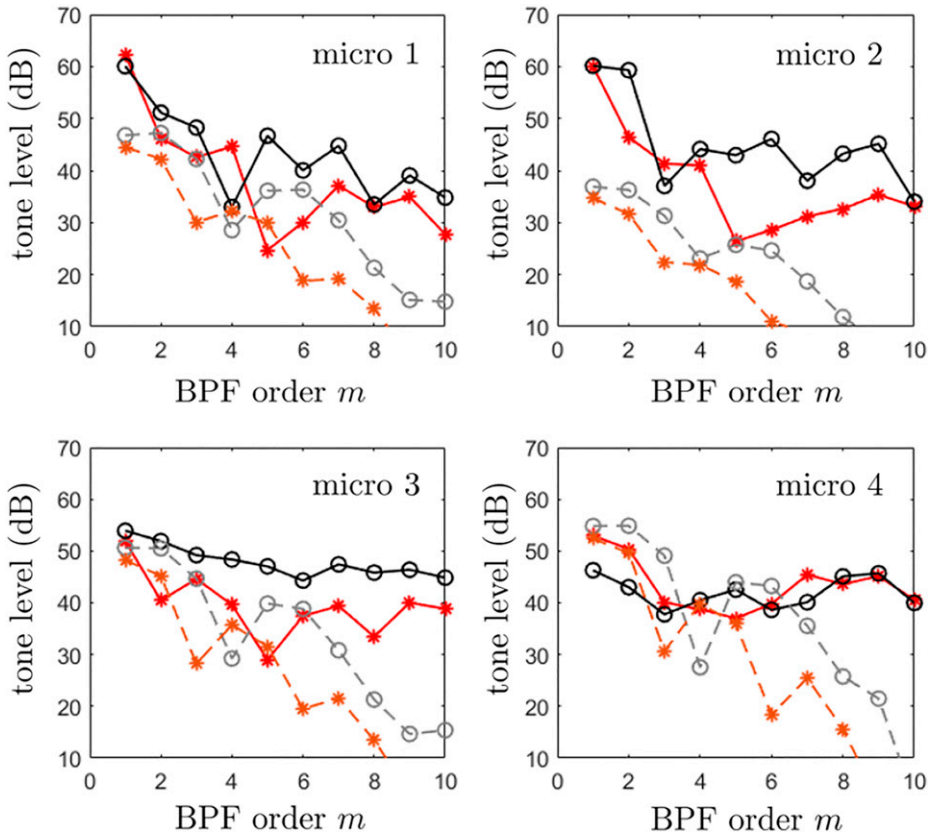
Figure 10. Measured tonal noise levels in cases 1 (red) and 2 (black), after integration over a bandwidth of 10 Hz, compared to model predictions (dashed brown: case 1, dashed gray: case 2).

nearly-zero BLH orders $s = \pm 18$. Some of these features are observed also in the measured sound spectra, in the installed configuration, typically on microphone 1 in case 2 and microphone 4 in case 1. More generally, drops in the measured tonal-noise envelope are shifted at other microphone positions, for two possible reasons. Firstly, other distortions than the wake of the wing are involved. Secondly, the wake has been characterized in the wing-alone configuration. The propeller probably distorts the wake features by adding momentum in the velocity deficit, which is not accounted for in the present analysis. The relative extinction of some tones appears as a specific feature of wake–propeller interaction in the investigated installed configurations.

Local sound predictions are compared to the measurements in Figure 10, for cases 1 and 2, and the microphone positions 1 to 4. The predictions are based on the free-field formulation, whereas the measurements include the effect of wing scattering. Yet first similarities and discrepancies can be identified. The higher-order BPF harmonics, of orders 6 to 10 or 8 to 10 depending on the microphone position, are systematically under-estimated. This suggests that they are produced by other distortions than the wing wake. The lower harmonics are better recovered, except for the microphone position 2, for which the predictions surprisingly remain about 20 dB below the measured levels. In fact, this microphone is close to the rotation plane, where the sound reaches its theoretical minimum, as shown by the directivity diagrams in Figure 9. Again, other sources than
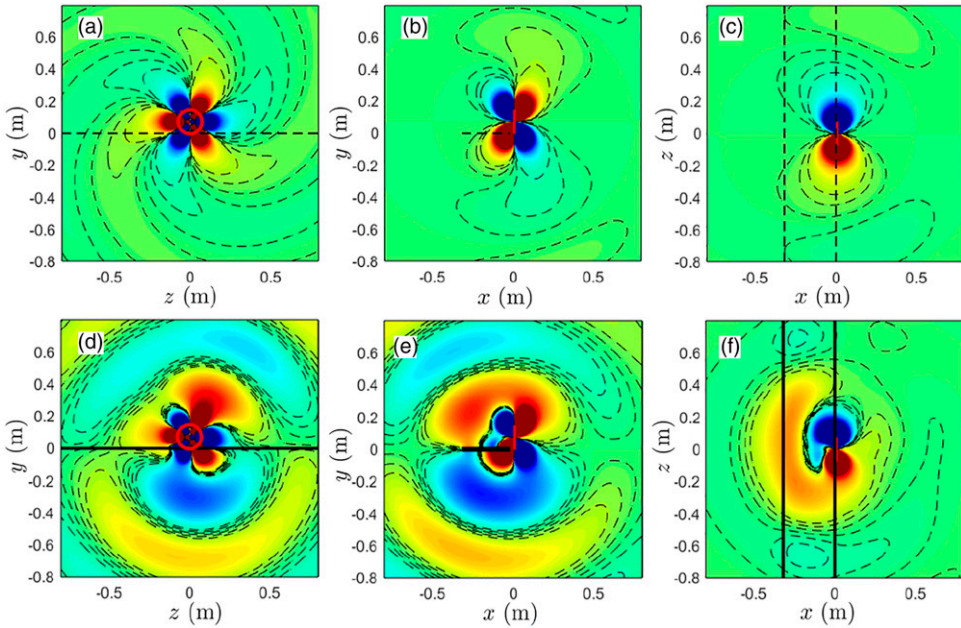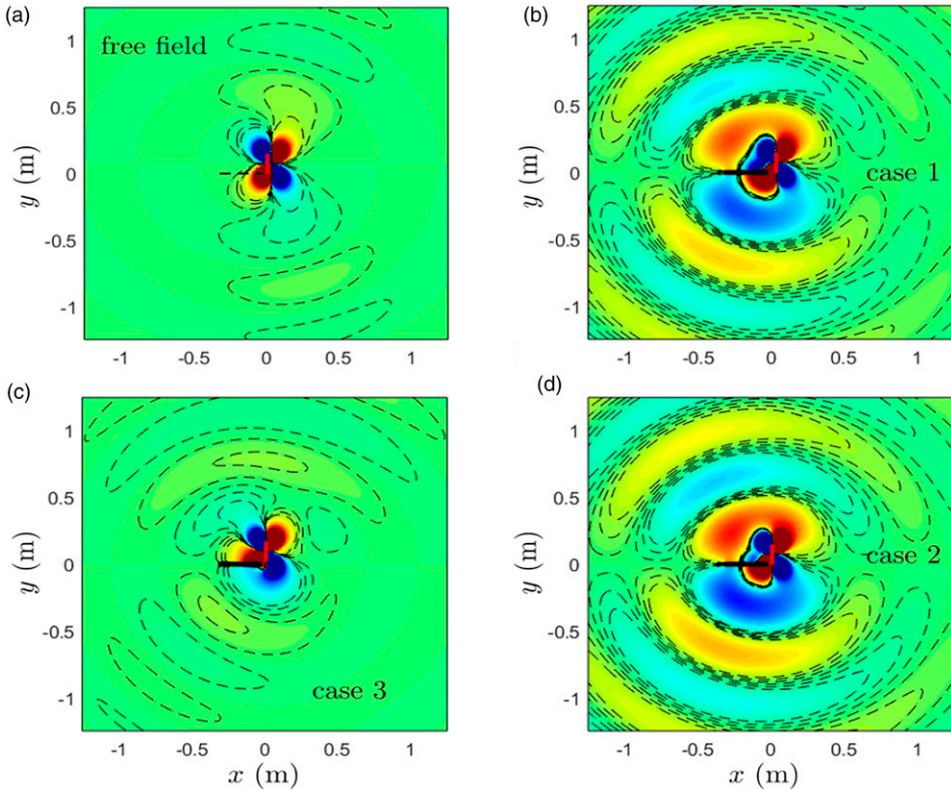
Figure 11. Instantaneous sound-pressure maps for the cumulative steady-loading noise sources, according to data in Table 2 (distributed mode n = 3). Free-field (upper plots) and in the presence of the wing, case 2 (lower plots). Same color scale on all plots, green for zero sound pressure and red and blue for over- and under-pressures, respectively. Six iso-contours over 10% of the maximum range.

wake interaction could contribute in this angular range. But, as confirmed later on, the most probable explanation of the discrepancies is the modification of the directivity induced by the scattering. Tones up to the seventh BPF harmonic have a maximum on axis, trace of the dominant zero-order radiation mode featured by the Bessel function J_0. The contribution of this mode drops at higher harmonics, leading to a local minimum on axis, and oblique radiation lobes. On the one hand, as a free-field lobe impinges on the edge, significant sound is regenerated in the shadow region because the edge becomes an efficient secondary emission point. In contrast, a main lobe radiating away from the edge is less disturbed. On the other hand, a direct sound path from source to observer corresponds to a strong or a weak scattering effect, depending on whether it is cut by the wing or not, respectively. This explains that the free-field predictions are somewhat closer to the measured sound for the microphone 4. The results for the microphone five are not reported for conciseness. They have been found close to those at microphone 4, and are of limited interest with regards to applications in which observers are on the ground.

Modal edge-scattering predictions

Analysis of near-field wavefront patterns. Instantaneous, near-field sound-pressure maps for the rotor-locked mode $n = B = 3$, associated with steady-loading noise at the BPF, are shown in Figure 11, in complementary perpendicular planes, namely the propeller plane $X = 0$ (a, d), the meridian plane $z = 0$ (b, e) and the wing plane $y = 0$ (c, f). Both the free-field radiation and that of the installed configuration, case 2, are compared. Because of the low tangential Mach number, this mode only
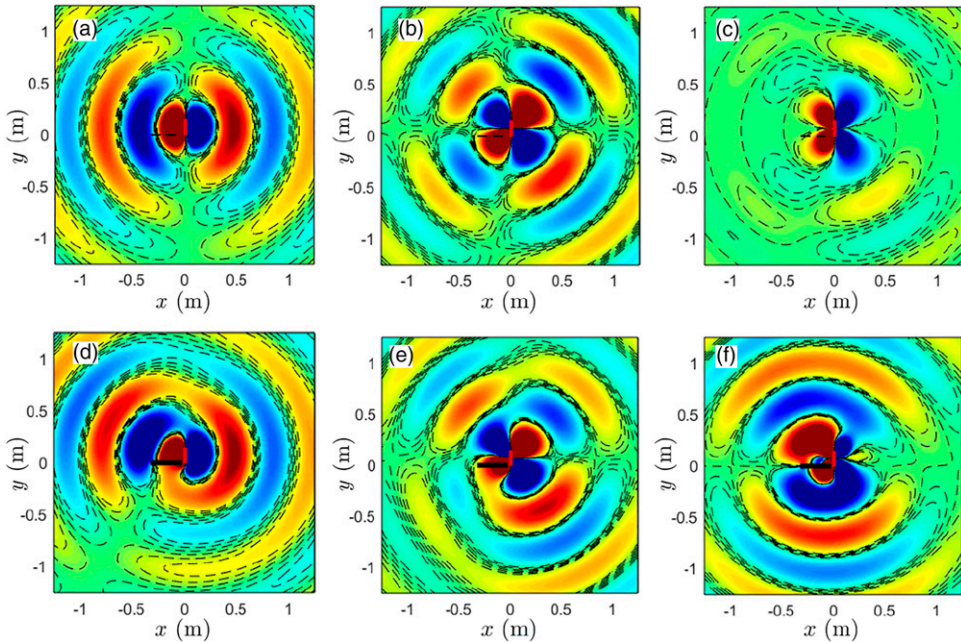
Figure 12. Instantaneous sound-pressure maps for the cumulative steady-loading noise sources, according to data in Table 2 (distributed mode n = 3). Trace in the meridian plane z = 0. Free-field (a) and in the presence of the wing, cases 1 (b), 3 (c) and 2 (d). Same color scale on all plots, green for zero sound pressure and red and blue for over- and under-pressures, respectively. Six iso-contours over 10% of the maximum range.

generates an evanescent wave in free field. The radiation is strongly enhanced in the presence of the wing, because of the vicinity of the scattering edge. The scattered field features large lobes, characteristic of an equivalent lift dipole. In this case, the distance of a part of the blade-tip circular path to the edge is much smaller than the wavelength, leading to a theoretical condition for amplification according to the asymptotic form of the Green's function. This suggests that, for the installed propeller, the steady-state aerodynamics of the blades radiates significant sound, whereas it is rather ineffective in ideal free-field conditions.

Figure 12 compares maps for the mode 3 of steady-loading noise at the BPF, in free-field and in the three installed configurations, in the meridian plane. Significant amplification is found in cases 1 and 2 but only a weak effect of the wing is found in case 3, despite the fact that the blade-tip to edge distance is larger for case 1 than for case 3. This is attributed to the dipole nature of the blade forces acting as sound. In case 3, the edge enters the angular range of local near-field extinction, whereas in cases 1 and 2 it enters a near-field lobe. This stresses the high sensitivity of the amplification mechanism.

Instantaneous pressure maps of modes 0, 1 and 2 at the BPF, again in the meridian plane normal to the wing, are shown in Figure 13, comparing the free-field to the close-to-the-edge installed

Figure 13. Typical instantaneous sound-pressure maps for source modes at the tip radius, in free field (a, b, c) and in installed configuration, case 2 (d, e, f). Traces in the meridian plane z = 0. Modes 0 (a, d), 1 (b, e) and 2 (c, f). Same arbitrary color scale for both plots of a mode (amplitudes 25 (mode 0), 5 (mode 1), 2 (mode 2)), indicative iso-contours, green for zero sound pressure and red and blue for over- and under-pressures, respectively.

configuration, case 2. The different color scales used in Figure 13(a)–(f) stress that, with the present parameters, the mode 1 is intrinsically much less effective than the mode 0 but more effective than the mode 2. In this plane, the free-field radiation of the mode 0 is that of an equivalent axial dipole, with an extinction plane normal to the propeller axis. In the presence of the wing, the extinction in the upper part of the map is only relative, and the extinction angle in the lower part is shifted to the left. This effect must taken into account to analyze the measured sound at the microphone position 1. The free field of the mode 1 exhibits an asymmetric four-lobed pattern, with oblique extinction angles almost normal to the axis (Figure 13(b)). In the presence of the wing, a single wide lobe tends to form in the lower half of the map, whereas two lobes are still identified in the upper part, with partial extinction in a tilted direction. Finally, the free-field pattern of the mode 2 is symmetric, as expected for an even order. It also features a four-lobed pattern, with two dominant oblique lobes on the right and two vanishing ones on the left. But the scattered field radiated from the wing is that of distributed lift dipoles, with opposite phases in the upper and lower half-maps. Furthermore, it is of significantly higher amplitude in this case. Therefore, the total field combines symmetric and anti-symmetric contributions, and roughly corresponds to that of a vertical dipole, except in the very near field of the propeller disc. It also appears that the modes 0 and 1 radiate sounds of similar amplitudes in free-field and installed configurations, whereas the mode 2 undergoes amplification, with a much more pronounced change of directivity. These basic modal features help to understand why the effect of edge scattering strongly differs, depending on the microphone position, even if combining several modes a priori tends to smooth angular variations. In the conditions of the experiment, the

Table 3. Approximate tonal-noise level differences, in decibels. Cumulative mode $n = 3$. Free-field subtracted from the total field in installed configuration.

	Case 1	Case 2	Case 3
Mic. 1	>20	20	6.5
Mic. 2	14	16	~0
Mic. 3	9	13	~0
Mic. 4	14	18	7.5

mode orders 0, ±1 and ±2 are the ones selected as the dominant contributors to the far-field sound by the Bessel-function filtering at the BPF (at least if they are forced by BLH of sufficient strength, see equation (2)). This is why the basic results illustrated in Figure 13 are key elements when trying to reproduce the measured sound at the BPF with analytical predictions. It is also worth noting that, in all maps of Figure 13, the zero sound on axis characteristic of free-field higher-order modes is essentially preserved in the presence of the wing, because the latter is quite close to the propeller axis.

Correction of free-field predictions

Apart from their interest to highlight the formation of wavefronts from the sources, the afore-mentioned computed maps also give access to an indicator of the scattering effect. For this, the difference in decibels is made between the acoustic fields computed with and without the wing. This difference provides a correction, to be applied to the free-field predictions. It is reported in Table 3, for the steady-loading noise at the BPF, and for the four microphone positions, 1 to 4. A similar analysis could be repeated for higher harmonics of the tonal noise, and for the wake-interaction noise as well.

A strong amplification is found in cases 1 and 2, at the microphone location 1, theoretically exceeding 20 dB. This prediction might be inaccurate, in particular because additional scattering is expected from the nozzle lips, quite close to the leading edge of the wing, as seen in Figure 5. Yet, a large increase is expected with respect to the free-field prediction at the same point. Another large increase is expected at the microphone location 4. Though the free-field estimates of steady-loading noise are of limited accuracy, adding the values of Table 3 leads to a reasonable overall agreement with the measured BPF tone levels in Figure 8. This suggests that steady-loading noise is, at least partly, responsible for the emission at the BPF.

Table 4 reports the same indicator, computed for the isolated source-modes of orders 0, 1 and 2, again at the BPF, and only for the radius of the blade-tip segment, in configuration case 2, from Figure 13. The radiation of the modes 0 and 1 is almost unaffected at the microphone positions 1 and 4, corresponding to angles relatively close to the propeller axis. In contrast, some amplification is noted for the same modes at the positions 2 and 3. The strong increase at the position 2 is due to the angular shift of the extinction angle seen in Figure 13(a), and (d). The radiation of the mode 2 is substantially enhanced in all directions, obviously involving the amplification mechanism.

As a final step, the complete fields radiated at the BPF by the blade-tip segments interacting with the wake are compared in Figure 14, according to the free-field and corrected predictions. For this test, only the modes able to contribute to the far field are accounted for. They are the modes $n = -2, -1, 0, 1, 2$, associated with the BLH of orders $s = 5, 4, 3, 2, 1$, respectively. The single-mode radiation patterns illustrated in Figure 13 have been simply summed, once weighted by their BLH

Table 4. Level differences of individual modes and of the complete tonal noise at the BPF due to wake interaction, in decibels. Free-field subtracted from the total field in installed configuration, case 2.

	$n = 0$	$n = 1$	$n = 2$	BPF tone
Mic. 1	~0	0.5	>20	~0
Mic. 2	16	6	13	9
Mic. 3	4	3	6.5	4
Mic. 4	~0	~0	4	~0
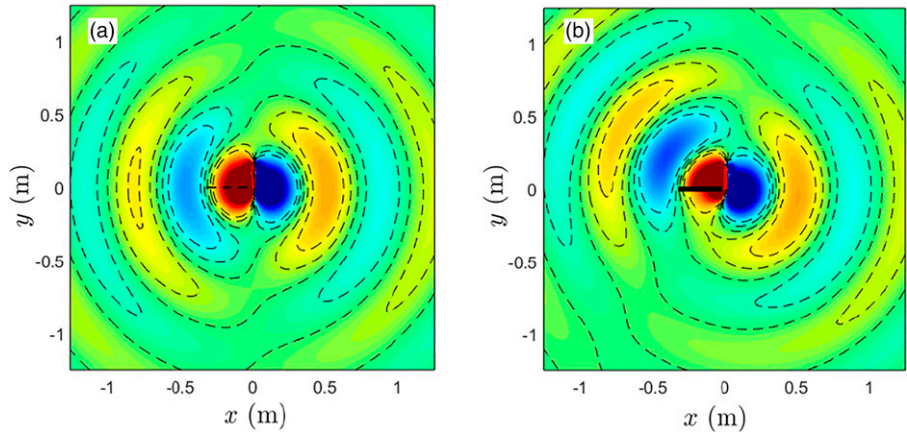
Figure 14. Instantaneous sound-pressure maps of the complete wake-interaction noise in the meridian plane $z = 0$. Combined modes $n = -2$ to $+2$, blade-passing frequency 495 Hz. Tip blade segment only. Free-field (a) versus case 2 (b). Same arbitrary color scale, green for zero sound pressure and red and blue for over- and under-pressures, respectively. Six iso-contours covering 25% of the maximum range.

amplitudes, noting that the modes $+n$ and $-n$ have the same characteristic features. The symmetric mode $n = 0$ imposes its dipole-like behavior in free field, by virtue of its strong radiating efficiency. The global wavefront pattern obtained in the presence of the wing has a similar shape, tilted in the clockwise direction. No global amplification is noticed, unlike the case of the steady-loading noise in Figure 11. Indeed, the mode $n = 2$ is the only one undergoing amplification, in view of the results presented in Figure 13(c), and (f), but it has a contribution of secondary importance. For completeness, the sound-level differences at the microphone positions 1 to 4 associated with the results in Figure 14 have been reported in Table 4. They are nearly zero for the positions 1 and 4, and only 9 dB at the position 2. This cannot reduce the large difference of more than 20 dB noted in Figure 10. It is conjectured that another source than the wake interaction is responsible for the noise radiation in the corresponding direction.

Conclusions

A two-step analytical prediction method has been presented, dedicated to the tonal noise of a propeller, the blade tips of which operate in the near wake of a thin rectangular wing of large aspect ratio. Firstly, the direct sound generation from the blade forces is calculated in free field, from a pre-determined velocity deficit in the wake. Secondly, the scattering of that sound by the wing is

calculated, by making use of the exact half-plane Green's function in a uniformly moving fluid. Estimates are also provided for the steady-loading noise, associated with the thrust and torque of the propeller. In view of the moderate chord-to-wavelength ratios encountered in practical applications, assuming a semi-infinite wing is inappropriate. A simple correction procedure has thus been implemented in order to account for a finite chord length. The validity of the correction has been established by preliminary tests not detailed here. It still needs to be confirmed by more extended comparisons with reference numerical simulations. The modal structure of the tonal noise allows to introduce source-modes as elementary circular distributions of phased dipoles. The scattering by the trailing edge is assessed directly on these modes, leading to a clear identification of the expected effects on the tonal noise.

An accompanying experiment has been carried out in a low-speed, open-jet anechoic facility, aimed at evidencing some specific features of edge scattering. For this, a small-scale drone propeller has been tested close to the edge of an airfoil mimicking the wing, in the flow delivered by the nozzle. In view of the didactic character of the experiment, a minimum instrumentation has been retained, including a Pitot probe and far-field microphones distributed in a meridian plane of the propeller, normal to the wing. The measured tonal-noise levels have been compared to free-field predictions based on a measured wake velocity deficit, without corrections accounting for edge scattering. Most predictions were underestimated by a couple of decibels, and up to 20 dB at angles close to extinctions angles of the free field. The amount of scattering has been modeled separately, explaining the underestimates produced by the free-field predictions. It is worth noting that the distortion-induced noise and the addressed acoustic installation effect combine in an intricate way. The installation effect is hard to isolate in an experiment, because it is specific to the modal structure of the tonal noise, associated with the aforementioned source-modes. Reproducing modes with neither flow nor propeller is possible in principle, resorting to a spinning-mode simulator, made of an array of phase-driven electro-acoustic sources. However, the intrusiveness of the supporting structure of the simulator would be detrimental to reliable measurements, especially with regards to the small size of the present experiment. A dedicated experimental study in air at rest with a spinning-mode simulator at larger scale could be the matter for a future work.

The major outcome is that the sound radiation from rotating-blade forces is significantly increased because of the vicinity of the wing, at least with the presently investigated ranges of parameters. Now the installation of propellers close to the trailing edge of a wing is a key aspect of distributed propulsion systems identified as candidates for future flying architectures. It goes with a possible reduction of drag by compensation of the velocity deficit in the wake. The present simple modeling approach enables to assess the acoustic counterpart, by providing orders of magnitude of the installation effects. The different modal contents of rotor-wake interaction and of steady-state aerodynamics as sound generating mechanisms correspond to very different wing scattering effects. Interaction noise dominantly involves the symmetric radiation mode, which is also the less affected by edge scattering. In contrast, steady-loading noise only involves rotor-locked modes, with zero contribution on axis. These modes are found strongly amplified by edge scattering in the present study. The reasons for sound increase appear to depend on the source mechanism. Essentially, wake-interaction noise is increased as the propeller is placed closer to the edge because of the aerodynamic installation effect: the wake is thinner and deeper. In contrast, steady-loading noise is increased as the propeller enters the amplification regime of edge scattering, which is an acoustic installation effect. The same effects are likely to be observed in similar configurations at larger scales and higher Mach numbers, that could be designed in aeronautics. They lead one to reconsider the ranking of steady-loading and unsteady-loading noise contributions, at the benefit of the former.

ORCID iDs

Michel Roger https://orcid.org/0000-0001-9067-011X
Daniel Acevedo-Giraldo https://orcid.org/0000-0002-1861-2393
Marc C Jacob https://orcid.org/0000-0001-5946-6487

References

1. Ffowcs Williams JE and Hawkings DL. Sound generation by turbulence and surfaces in arbitrary motion. *Philos Trans R Soc Lond Ser A, Math Phys Sci* 1969; 264(1151): 321–342.
2. Lighthill MJ. On sound generated aerodynamically i. general theory. *Proc R Soc Lond Ser A. Math Phys Sci* 1952; 211(1107): 564–587.
3. Curle N. The influence of solid boundaries upon aerodynamic sound. *Proc R Soc Lond Ser A. Math Phys Sci* 1955; 231(1187): 505–514.
4. Williams JF and Hawkings D. Theory relating to the noise of rotating machinery. *J Sound Vibrat* 1969; 10(1): 10–21.
5. Lowson M. The sound field for singularities in motion. *Proc R Soc Lond Ser A. Math Phys Sci* 1965; 286(1407): 559–572.
6. Cros E, Roger M and Serre G. On the very low frequency scattering of propeller noise by a neighboring cylinder. In: AIAA AVIATION 2021 FORUM, VIRTUAL EVENT, 2–6 August 2021, 2021, p. 2251.
7. Howe MS and Howe MS. *Theory of vortex sound*. Cambridge: Cambridge University Press, 2003.
8. Williams JF and Hall L. Aerodynamic sound generation by turbulent flow in the vicinity of a scattering half plane. *J Fluid Mech* 1970; 40(4): 657–670.
9. Roger M, Moreau S and Kucukcoskun K. On sound scattering by rigid edges and wedges in a flow, with applications to high-lift device aeroacoustics. *J Sound Vibrat* 2016; 362: 252–275.
10. Roger M. Broadband noise from lifting surfaces analytical modeling and experimental validation. In: *Noise Sources in Turbulent Shear Flows: Fundamentals and Applications*. Vienna: Springer, 2013, pp. 289–344.
11. Roger M and Moreau S. Aeroacoustic installation effects in cooling fan systems part 1: scattering by surrounding surfaces. In: Proceedings of the International Symposium on Transport Phenomena and Dynamics of Rotating Machinery, Honolulu, HI, USA, 2008, pp. 17–22.

12. Roger M and Moreau S. Tonal-noise assessment of quadrotor-type uav using source-mode expansions. In: *Acoustics*. Basel, Switzerland: Multidisciplinary Digital Publishing Institute, 2020, 2, pp. 674–690.

13. Roger M and Kucukcoskun K. Near-and-far field modeling of advanced tail-rotor noise using source-mode expansions. *J Sound Vibrat* 2019; 453: 328–354.

14. Jones D. Aerodynamic sound due to a source near a half-plane. *IMA J Appl Math* 1972; 9(1): 114–122.

15. Rienstra S. Sound diffraction at a trailing edge. *J Fluid Mech* 1981; 108: 443–460.

16. Macdonald H. A class of diffraction problems. *Proc Lond Math Soc* 1915; 2(1): 410–427.

17. Noble B and Weiss G. Methods based on the wiener-hopf technique for the solution of partial differential equations. *Phys Today* 1959; 12(9): 50.

18. Howe MS. Edge-source acoustic green's function for an airfoil of arbitrary chord, with application to trailing-edge noise. *Q J Mech Appl Math* 2001; 54(1): 139–155.

19. Beriot H. *Personal communication*, 2001.

20. Intaratep N, Alexander WN, Devenport WJ, et al. Experimental study of quadcopter acoustics and performance at static thrust conditions. In: 22nd AIAA/CEAS Aeroacoustics Conference, Lyon, France, 30 May–1 June, 2016, p. 2873, 2016.

21. Misiorowski M, Gandhi F and Oberai AA. Computational study on rotor interactional effects for a quadcopter in edgewise flight. *AIAA J* 2019; 57(12): 5309–5319.

22. Goldstein ME. *Aeroacoustics*. New York: McGraw-Hill International Book Co, 1976.

23. Ventura Diaz P and Yoon S. High-fidelity computational aerodynamics of multi-rotor unmanned aerial vehicles. In AIAA SciTech Forum, Kissimmee, Florida, 8–12 January 2018, 2018.